



CHORUS

This is the accepted manuscript made available via CHORUS. The article has been published as:

Micrometer-Scale Magnetic-Resonance-Coupled Radio-Frequency Identification and Transceivers for Wireless Sensors in Cells

Xiaolin Hu, Kamal Aggarwal, Mimi X. Yang, Kokab B. Parizi, Xiaoqing Xu, Demir Akin, Ada S. Y. Poon, and H.-S. Philip Wong

Phys. Rev. Applied **8**, 014031 — Published 26 July 2017

DOI: [10.1103/PhysRevApplied.8.014031](https://doi.org/10.1103/PhysRevApplied.8.014031)

Micron-scale magnetic resonant coupled RFID and transceivers toward wireless sensors in cells

Xiaolin Hu,¹ Kamal Aggarwal,^{1,2} Mimi X. Yang,¹ Kokab B. Parizi,¹
Xiaoqing Xu,^{1,3} Demir Akin,⁴ Ada S. Y. Poon,¹ and H.-S. Philip Wong¹

¹*Department of Electrical Engineering, Stanford University, Stanford, California 94305, USA*

²*Qualcomm, San Jose, CA 95110*

³*Stanford Nanofabrication Facility, Stanford University, Stanford, California 94305, USA*

⁴*Center for Cancer Nanotechnology Excellence, Stanford University, Stanford, California 94305, USA*

(Dated: June 27, 2017)

We report the design, analysis and characterization of a three-inductor radio-frequency identification (RFID) and transceiver (TRX) system for potential applications in individual cell tracking and monitoring. The RFID diameter is 22 μm and can be naturally internalized by living cells. Using magnetic resonant coupling, the system shows resonance shifts when the RFID is present and also when the RFID loading capacitance changes. It operates at 60 GHz with a high signal magnitude up to -50 dB and a sensitivity of 0.25. This miniaturized RFID with a high signal magnitude is a promising step toward continuous, real-time monitoring of activities at cellular levels.

I. INTRODUCTION

Continuous detection and manipulation of cellular activities can significantly advance our knowledge in biology and disease, and enable new discoveries in diagnostics and therapeutics. Various technologies have been developed to sense cellular activities and manipulate cells. Optical cavities have been demonstrated to record intracellular pressure [1]. Fluorescent dyes are available to monitor subcellular pH levels [2] and chloride concentrations [3]. Nanorod motors can be stimulated with acoustic waves to agitate outside or within living cells [4].

There has been an ongoing interest in making single-cell wireless radio-frequency identification (RFID) sensors and controllers as an alternative solution [5]. Since power and information are carried via electromagnetic waves, RFIDs can be used in both optically transparent and opaque settings. They can harvest energy to power up integrated circuits (IC) and sensors which can provide high sensitivity and versatile sensing modalities. RF-powered devices can be found in healthcare products and research tools, as in neuro-stimulators [6], pacemakers [7], glucose sensors [8], and medical adherence monitors [9]. These devices are typically on the scale of centimeters and millimeters and consequently impractical as means to address to individual cells. The sizes are usually dominated by large antenna receivers [5]. Nano-antennas made of carbon nanotubes have been attempted, but they cannot sense information or power up IC as most energy is dissipated through heat [10].

Other than RF devices, piezoelectric and electrostatic ultrasound-based devices are also explored as wireless miniaturized actuators, energy harvesters, and sensors. As they are electromechanical systems, they involve both mechanical impedance matching with surrounding media and electrical impedance matching with interface circuitry [11–13]. Both impedances are affected by device

geometry and the two requirements can conflict with each other. Moreover, often the signals are measured via direct probing or transferred via an additional RF link [14–17], hence the system is not truly wireless with just the electromechanical components.

Leveraging advances in nanofabrication and wireless engineering, we present a vision toward RF probing inside living cells with micron-scale RFID receivers [18]. The complete system schematic is shown in FIG. 1. The RFIDs are small enough to fit inside individual cells. They are fully encapsulated in SiO_2 for bio-compatibility [19]. The RFID-tagged cells are flown through a microfluidic channel made of polydimethylsiloxane (PDMS). Using magnetic resonant coupling, RFIDs are interrogated individually by the transceiver (TRX) right underneath the channel. With a coplanar waveguide transmission line (CPW TL) underneath the PDMS bulk, the TRX front end is connected to ground-signal-ground (GSG) pads. The pads are probed with a vector network analyzer (VNA) which serves as the power source and the measurement unit. The complete RFID would include an active IC sensor block which robustly translates the biological change $\Delta\theta$ to RFID load capacitance change ΔC_3 , subsequently shifting the resonance frequency by Δf in the VNA measured reflection coefficient S_{11} .

As a significant step toward a system enabling RF-based cell-by-cell wireless monitoring, we report the design, measurement, and analysis of the major electrical components including the RFID, TRX detector, and transmission line. This passive system can detect RFID presence and loading capacitance variation with high signal magnitude and sensitivity. Currently, the RFIDs are only 22 μm in diameter. They can be internalized inside cells and can function as tags to track the cells. The primary and secondary TRX loops are 50 and 40 μm in diameter, respectively. Instead of using a more straightforward and conventional two-loop design with only one inductive loop for the TRX detector, a third, intermediate loop detector is resonantly

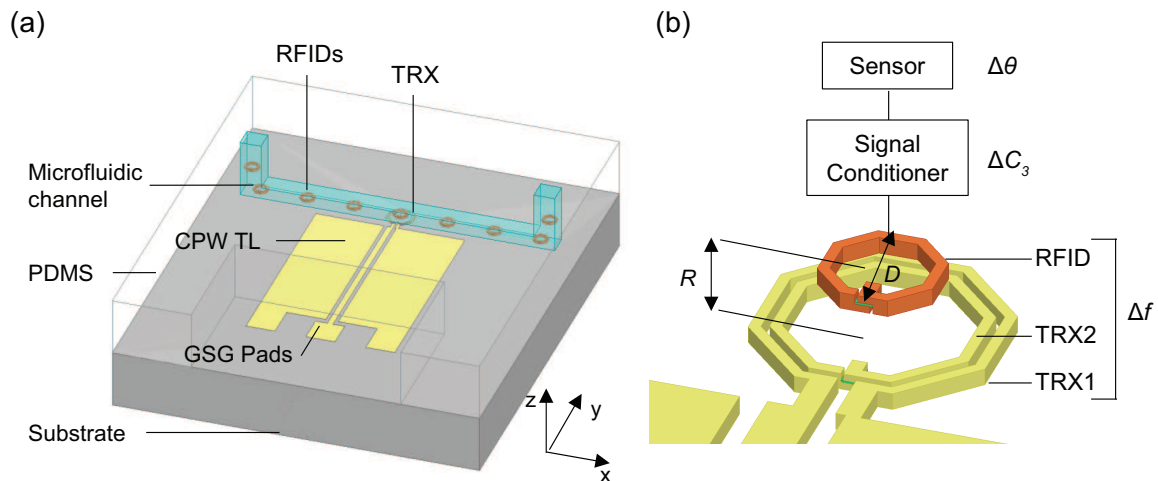


FIG. 1. Schematic illustrating the instrumentation for wireless communication with RFIDs in cells. (a) RFID-tagged cells are flown through a PDMS microfluidic channel and interrogated by the transceiver (TRX). The signal is probed through ground-signal-ground (GSG) pads connected to the TRX by a coplanar waveguide transmission line (CPW TL). (b) Enlarged schematic of the sensor, signal conditioner, and the three-inductor RFID/TRX wireless front end.

coupled with the RFID. This greatly enhances the signal magnitude from -2 dB to -50 dB [FIG. 3 (e),(f)]. A -2 -dB signal measured with stationary devices on chip will be nearly impossible to detect with moving RFIDs in the lossy biological solution environment. Extra intermediate inductors are known for improving power transfer efficiency and extending communication range [20–24]. This novel application of multi-inductor resonant coupling is essential for obtaining measurable signals with micron-sized devices. To the authors' knowledge, this RFID is the smallest developed so far.

The manuscript is organized as follows: Section II presents the analytical model for the design process. Section III describes the experimental methods for 3D simulations, RF measurements and cell internalization tests. Section IV evaluates the system performance with practical considerations, and we conclude in Section V. Detailed mathematical derivations for some equations in II are included in the appendix at the end.

II. THEORETICAL ANALYSIS

It is a challenge to design, fabricate, and characterize a small RFID that can fit inside cells. Many figures of merit can be considered for optimization such as device size, detection range, operating power level, signal magnitude, signal-to-noise ratio, and so on. For our application, the device size and detection range have already been set. We limit the RFID diameter to be less than $25 \mu\text{m}$, which is the typical size of mouse macrophages that have previously been demonstrated to internalize similar dummy RFID structures [19]. Since the RFIDs are flown through a thin microfluidic channel above the TRX detector, the detection range is a few micrometers. In operation, we need to determine if

the RFID is present and if its loading capacitance is changing. These changes are indicated by resonance frequency shifts. Therefore, signal magnitude near the resonance is our first figure of merit as strong signals are the prerequisite for measurements. However, with our constraints, it is difficult to achieve sufficient signal magnitude using common designs with a single inductive detector. Devices smaller than cells can only be made of thin metal wires with limited cross-sectional areas. Compared to large devices made of thicker metal wires, they have higher Ohmic loss. Also, the aqueous working environment inherent to biological applications causes dielectric loss. In addition, characterization of small RF devices is vulnerable to measurement and post-processing errors. Apart from the signal magnitude, the other key figure of merit is the sensitivity σ , which is the degree of resonance frequency shift when the loading (the biological signal to be sensed) changes.

In search for an optimal RFID design and detector geometry feasible with current fabrication technology, we need to explore the design space that includes the inductor diameter, cross-section geometry, and operating frequencies. Analytical modeling of the system using the Method of Moments [25] is employed to quickly sweep through design these design parameters and to cross-check simulation results.

A. Analytical Framework

The RFID/TRX is analyzed following the steps outlined in ref. [25] using custom MATLAB[®] code [26]. We started to solve for two-loop designs as in [25], but the signal magnitude thus obtained was insufficient [FIG. 3 (b)]. Hence we extend the method to solve for the three-loop structures in this work shown in FIG. 2. The

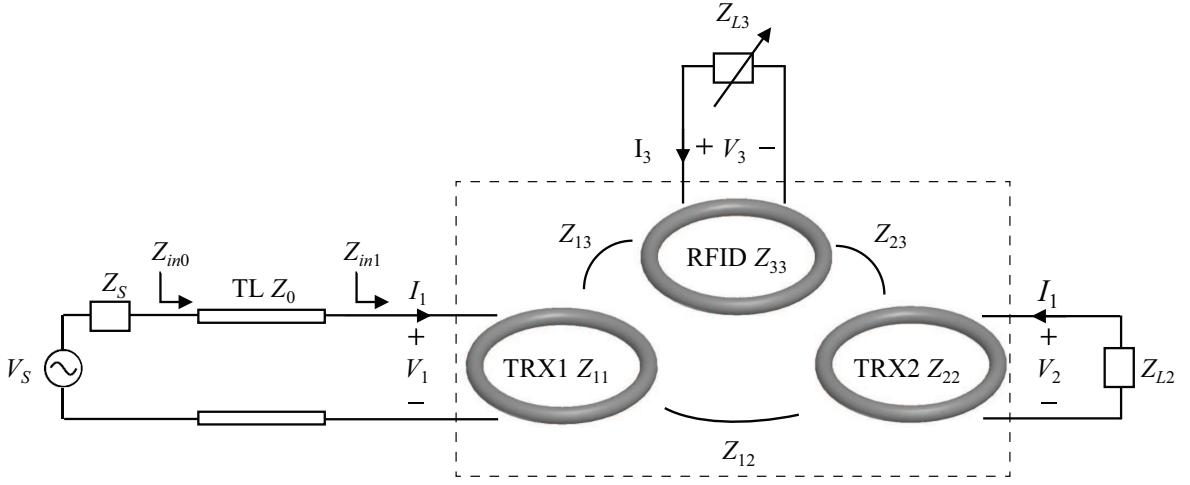


FIG. 2. Models the coupling among the multiple-loop RFID/TRX as a three-port network, \mathbf{Z} . The self-impedance terms are considered as an inductor in series with a resistor. The mutual impedance terms represent the mutual inductance. The load impedances are capacitors that cancel out TRX2 and RFID inductors at the same resonance frequency.

RFID/TRX loops are approximated as concentric rings with rectangular cross-sections immersed in water. The RFID/TRX are modeled as a three-port network \mathbf{Z} as in Eq. (1 a-c). The secondary TRX2 loop and RFID are connected to load Z_{L2} and Z_{L3} which are capacitors in our case, and Z_{L3} can be modulated by a sensor. The primary TRX1 loop is connected to the VNA through a transmission line (TL) with characteristic impedance Z_0 . The VNA is modeled as a voltage source with impedance Z_S . Reflection coefficient Γ is the signal of interest. Dielectric loss and skin effect are also considered.

$$V_1 = Z_{11}I_1 + Z_{12}I_2 + Z_{13}I_3, \quad (1a)$$

$$V_2 = -Z_{L2}I_2 = Z_{21}I_1 + Z_{22}I_2 + Z_{23}I_3, \quad (1b)$$

$$V_3 = -Z_{L3}I_3 = Z_{31}I_1 + Z_{32}I_2 + Z_{33}I_3. \quad (1c)$$

Referring to FIG. (2), maximum signal strength is obtained when Z_S is matched with Z_{in0} , the equivalent impedance seen into the TL. This can be done by quarter-wave transformation of Z_0 and Z_{in1} , the equivalent impedance seen into TRX1 [27]. However, this impedance transformation is narrow-band and the matching can be lost when Z_{L3} is varied. Also, impedance transformation only allows for limited fabrication variation which may shift the frequency response of the RFID/TRX. Thus, we match Z_0 with Z_S which can be achieved through a wide range of frequencies, and then focus on matching Z_{in1} with Z_S .

B. Mechanism for three-loop configuration

With matching Z_0 and Z_S , the reflection coefficient can be written as

$$\begin{aligned} \Gamma &= \frac{Z_{in1} - Z_0}{Z_{in1} + Z_0} \\ &= \frac{\Gamma_1 + \frac{Z_{2,3 \rightarrow 1}}{Z_{11} + Z_0}}{1 + \frac{Z_{2,3 \rightarrow 1}}{Z_{11}}} \end{aligned} \quad (2)$$

where $Z_{2,3 \rightarrow 1}$ is the equivalent impedance of TRX2 and RFID seen at TRX1, and Γ_1 captures the mismatch between TRX1 itself and Z_0 :

$$\Gamma_1 = \frac{Z_{11} - Z_0}{Z_{11} + Z_0}. \quad (3)$$

Typically, $Z_{2,3 \rightarrow 1}$ is small, so Γ is approximately equal to Γ_1 . However, in our case, $Z_{2,3 \rightarrow 1}$ is not small due to the extremely small separation among the loops relative to their sizes. Z_{11} is too small to match with a normal $Z_S = 50 \Omega$ and Γ_1 is approximately -1 . Equation 2 can be simplified to

$$\Gamma \approx \frac{\frac{Z_{2,3 \rightarrow 1}}{Z_{11} + Z_0} - 1}{\frac{Z_{2,3 \rightarrow 1}}{Z_{11} + Z_0} + 1} = \frac{Z_{2,3 \rightarrow 1} - Z_{11} - Z_0}{Z_{2,3 \rightarrow 1} + Z_{11} + Z_0} \approx \frac{Z_{2,3 \rightarrow 1} - Z_0}{Z_{2,3 \rightarrow 1} + Z_0}. \quad (4)$$

For our devices at micron-scale with small input impedances, we want to maximize $Z_{2,3 \rightarrow 1}$ to improve the matching. $Z_{2,3 \rightarrow 1}$ is simplified as

$$\begin{aligned} Z_{2,3 \rightarrow 1} &\approx \frac{|Z_{12}|^2}{Z_{22} + Z_{L2}} + \frac{|Z_{13}|^2}{Z_{33} + Z_{L3}} \\ &\quad - \frac{Z_{12}Z_{13}Z_{23}}{(Z_{22} + Z_{L2})(Z_{33} + Z_{L3}) - Z_{23}^2}. \end{aligned} \quad (5)$$

Since $Z_{ij} (i \neq j)$ is purely imaginary, the last term is imaginary and captures the interaction among all three

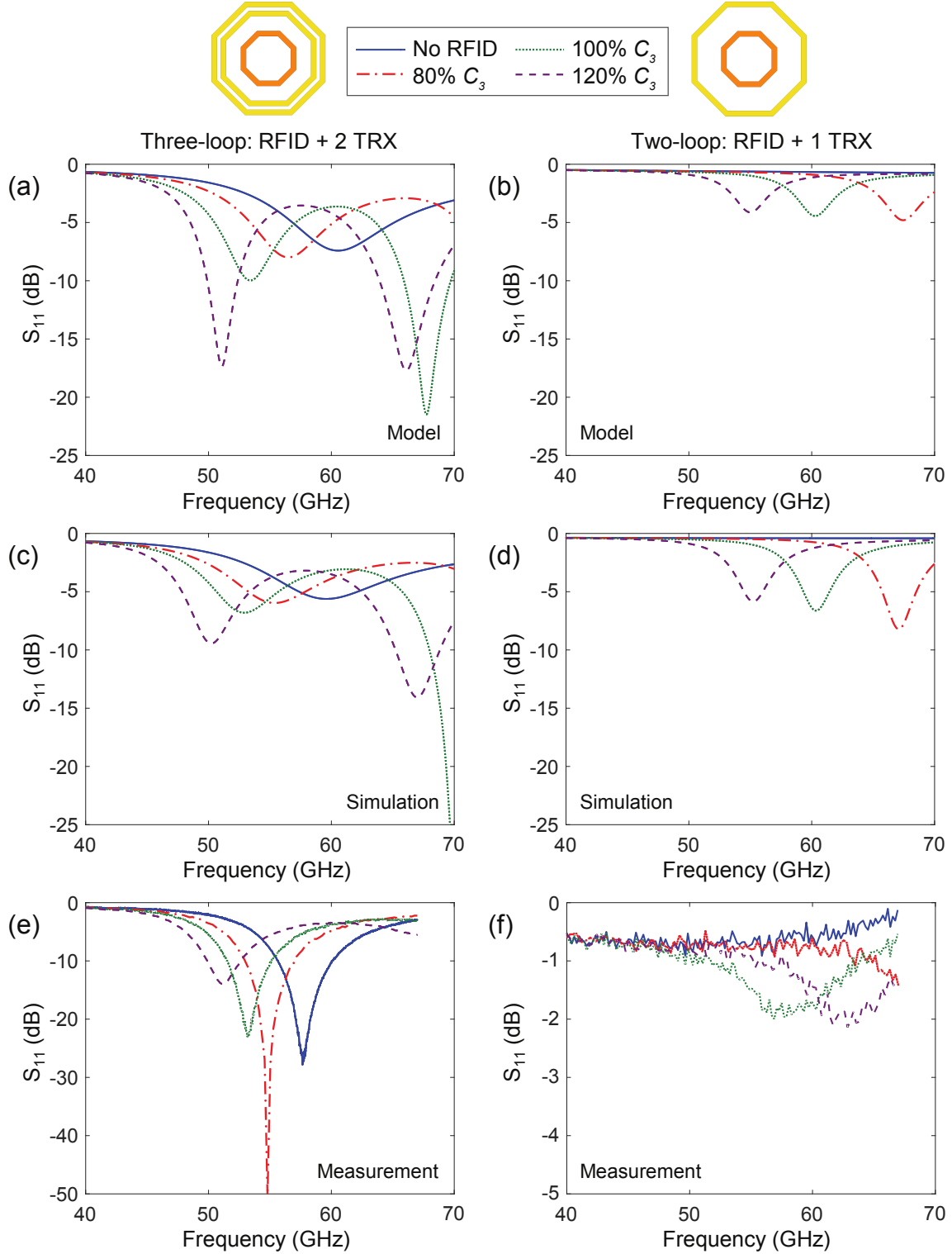


FIG. 3. Evolution of the RFID/TRX resonances in reflection coefficients S_{11} with RFID presence and its loading capacitance changes. With 100% C_3 , the RFID resonates at the same frequency with TRX2. (a, c, e) Three-loop data from analytical model, HFSS 3D EM simulation, and experimental measurement. (b, d, f) Corresponding two-loop data.

loops. The first two terms describe the direct loading effect of TRX2 and RFID on TRX1. They are real terms that shall be maximized to improve matching. Clearly, large mutual inductances are beneficial so we explore different loop geometries to maximize mutual inductances. Another straightforward way to enhance matching is to capacitively load TRX2 and RFID with close resonance frequencies so the denominators of the first two terms are minimized. Hence our three-loop system terminates TRX2 and RFID with capacitors.

Note that this three-loop structure has a much higher impedance near resonance versus a two-loop structure. A two-loop structure would only exhibit the second term of Eq. 5. This term contributes much less to the total impedance versus the first term as TRX1 and RFID only weakly couple.

We choose the resonance frequencies of TRX2 and RFID to be the same as ω_0 . In the absence of the RFID, the system has a resonance frequency ω_0 . When the RFID is present, TRX2 and RFID are over-coupled and resonance splitting occurs, shifting the overall resonance frequency. [20, 28–32]. The loading capacitance of RFID also shifts the resonance frequency [FIG. 3(a)]. If the lower resonance from the split is used as the signal marker, the sensitivity σ can be approximated as

$$\sigma_L = \frac{\Delta f/f}{\Delta C_3/C_3} = -\frac{1}{\sqrt{1+k_{23}}}. \quad (6)$$

k_{23} is their mutual inductance coupling coefficient. This predicts a relatively constant sensitivity across frequency as long as coupling coefficient k_{23} remains constant. As the RFID and TRX are coupled through near-field, the coupling coefficient is thus relatively constant within the frequencies of interest.

III. EXPERIMENTAL METHODS

A. Simulation and Fabrication

The MoM modeling is corroborated by EM simulation with ANSYS[®] HFSS [33]. More details are included in the EM simulation to mimic the actual fabrication process and testing environment. The detector and RFID loops are octagons with the same diameters used in MoM modeling. They sit on a SiO₂ coated silicon wafer covered in water. While the actual foundry process for the RFID and detector uses multiple oxide layers with various dielectric constants, a single block of SiO₂ coating with equivalent thickness is used to expedite the simulation [34]. The bottom of the silicon wafer is grounded with a perfect electric conductor-plane to terminate fields. Radiation boundaries are applied to other directions to allow EM wave to escape. For simplicity, the loads of RFID and TRX2 are modeled as ideal capacitors. Figure 3 (c)-(d) show the simulated three-loop and two-loop RFID/TRX performance. HFSS simulation

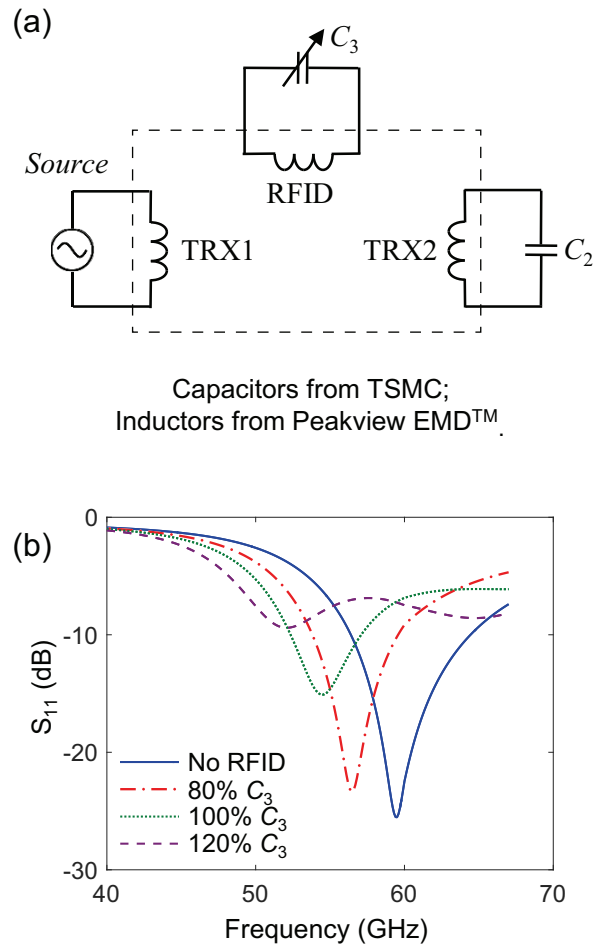


FIG. 4. The simulation setup (a) and simulation results (b) of the RFID/TRX fabricated using the TSMC 40-nm general process process. The inductors and capacitors models were extracted separately from Peakview EMD[™] and TSMC vendor models. The simulation results have similar resonance frequencies with models, HFSS simulations, and measurements in FIG. 3.

is also used to design the coplanar wave transmission line (CPW-TL) to derive the desired characteristic impedance.

To verify the design, the passive system is fabricated with TSMC (Taiwan Semiconductor Manufacturing Company, Ltd) 40-nm CMOS general process [35]. The RFID/TRX loops are made of a wide and thick copper layer. Simulations were performed to include even more details in the foundry process. Peakview EMD[™] software [36] is used to simulate the inductors on the actual foundry process stack with chemical mechanical planarization (CMP) fill shapes placed around. Metal-oxide-metal (MOM) structures are used as loading capacitors. Their capacitances and losses are accounted for in the foundry model. Combining the Peakview EMD[™]-generated inductor models and the foundry-generated capacitor models, we simulate the RFID/TRX from the foundry using Cadence[®] Spectre[®]

[37] as in FIG. 4 (a). These simulations [FIG. 4 (b)] show similar resonant frequencies with MoM model, HFSS simulation, and electrical measurement.

B. Electrical Characterization

The RFID/TRX are characterized using Cascade infinity GSG probes and an Agilent VNA E8361A. As the final system consists of both the RFID/TRX front-end and the CPW TL, testing geometries are laid out to test them both separately and together. The TRX/RFID is measured with a two-port system shown in FIG. 5(a), where they are connected in series between two GSG probing pads. We used the Pad/Open/Thru dummy structures [38] to de-embed the measurement results [FIG. 5(a)].

The de-embedded S parameters were converted to Y parameters to calculate impedance at TRX1 [39]. As TRX1 is connected in series between the two measurement ports, its impedance and the loading from TRX2 and RFID can be calculated as

$$Z_{meas} = -\frac{2}{Y_{21} + Y_{12}}. \quad (7)$$

This impedance Z_{meas} is essentially Z_{in1} . Substituting it into Eq. 2, we can obtain Γ and S_{11} to mimic the situation when TRX/RFID is directly connected to VNA. The S_{11} was used to compare with modeling and simulation results [FIG. 3]. Note that the measured three-loop signal is stronger than the simulated and modeled data, because the model and simulation overestimate the input impedance Z_{in1} to be above 50 Ω , underestimating matching and signal strength. The Ohmic losses in the metal and dielectric losses in the substrate limit the maximum impedance that can be attained on the chip.

We also measured the structure of RFID/TRX with 300- μm -long CPW TL [FIG. 5(b)]. Recall in FIG. 1, it is necessary to connect the TRX structure underneath microfluidic channel to the exposed RF probing pads outside the PDMS slab. The PDMS slab surrounding the microfluidic channel can be diced to a width of a few hundred micrometers, therefore these long CPW TLs are needed to bridge the TRX and probing pads. These are the structures needed for the actual application. The result in FIG. 5(c) matches with that of TRX/RFID alone in FIG. 3(e), in agreement with the low-loss nature of the transmission line and good impedance matching between the line impedance and Z_{in1} .

C. Biocompatibility Verification

To test the biocompatibility of the RFID, the confluent culture of mouse melanocytic melanoma cells was incubated with RFID tags for 42 hours and imaged at intervals of three minutes to capture cell uptake of the RFID chips in a procedure described in [19]. The

cell concentration was about 2×10^3 cells/mL, and the RFID-to-cell ratio was about 1 to 1. FIG. 6 shows time-elapse images demonstrating RFID internalization and cell persistence. The complete video is included in the supplemental material [40].

The RFIDs presented in the previous sections were aimed at verifying the various designs for the RFID and the TRX. To study the biocompatibility of the RFIDs, it is necessary to fabricate a massive number of these RFIDs to allow experimentations of the cell handling and imaging conditions. We mass fabricated in-house versions of the RFIDs with the same diameter and the same resonant frequency at 60 GHz [FIG. 7] as the RFIDs from the silicon foundry. The house RFID fabrication and release processes are described in [18, 19]. In brief, these RFIDs consist of two metal layers sandwiching a thin dielectric layer. The first metal layer is 5 nm titanium and 200 nm gold functioning as a bottom capacitor electrode. The second metal layer is 1000 nm aluminum functioning as a top capacitor electrode and inductor loop. The capacitor dielectric layer is 16 nm of HfO_2 for RFID at 60GHz. The devices are fabricated on Si wafers and fully encapsulated by SiO_2 for biocompatibility.

IV. SYSTEM DESIGN VALIDITY

In the previous sections, we have successfully demonstrated the design, fabrication, and electrical and biological characterizations of a RFID/TRX wireless link, suitable to be embedded into living cells. The RFID/TRX operates near 60 GHz. It exhibits strong measured signal magnitudes up to -50 dB with a capacitive sensitivity of 0.2. These are promising results toward implanting RFIDs into cells to monitor cell activities wirelessly.

A few more questions need to be addressed before realizing the practical system depicted in FIG. 1. First, is 60 GHz the optimum operating frequency to maximize signal strength or sensitivity? Next, each RFID will no longer be stationary and concentric with the TRX. The RFID will be a few micrometers afloat above the TRX inside the microfluidic channel. The RFID will also be subjective to lateral misalignment from the TRX as the RFID drifts through the channel. How will the vertical and lateral displacements affect the signal detection? To validate the system design, we answer questions about frequency dependency, vertical detection range, and lateral detection range through MoM modeling and HFSS simulations in the following subsections.

A. Frequency Dependency

We have chosen the three-loop TRX/RFID configuration with a nominal operating frequency at 60 GHz. The operating frequency for implantable RF

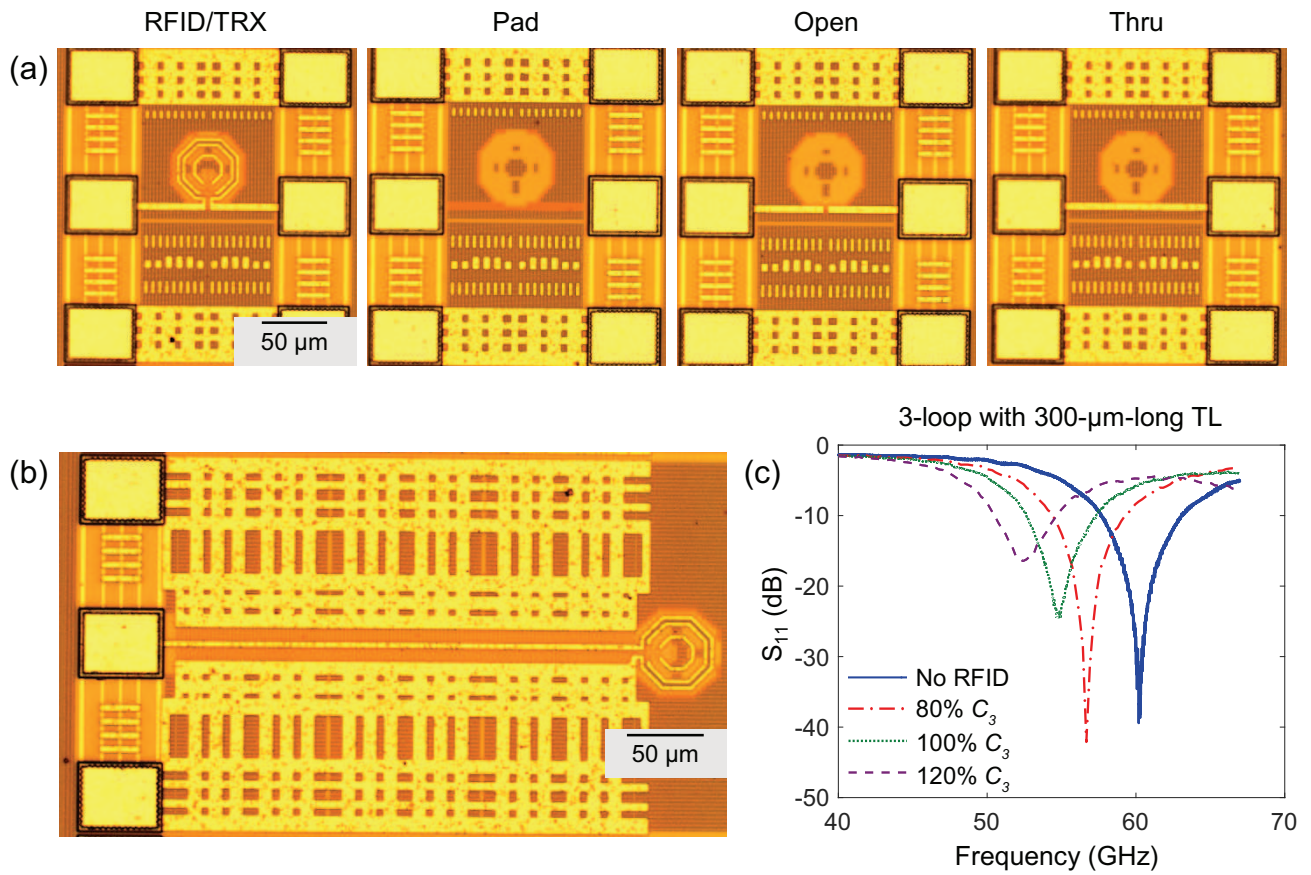


FIG. 5. (a) Measurement structures for RFID/TRX and de-embedding structures. (b-c) Measurement structure and results for the 3-loop RFID/TRX connected with a 300 μm-long CPW TL attached.

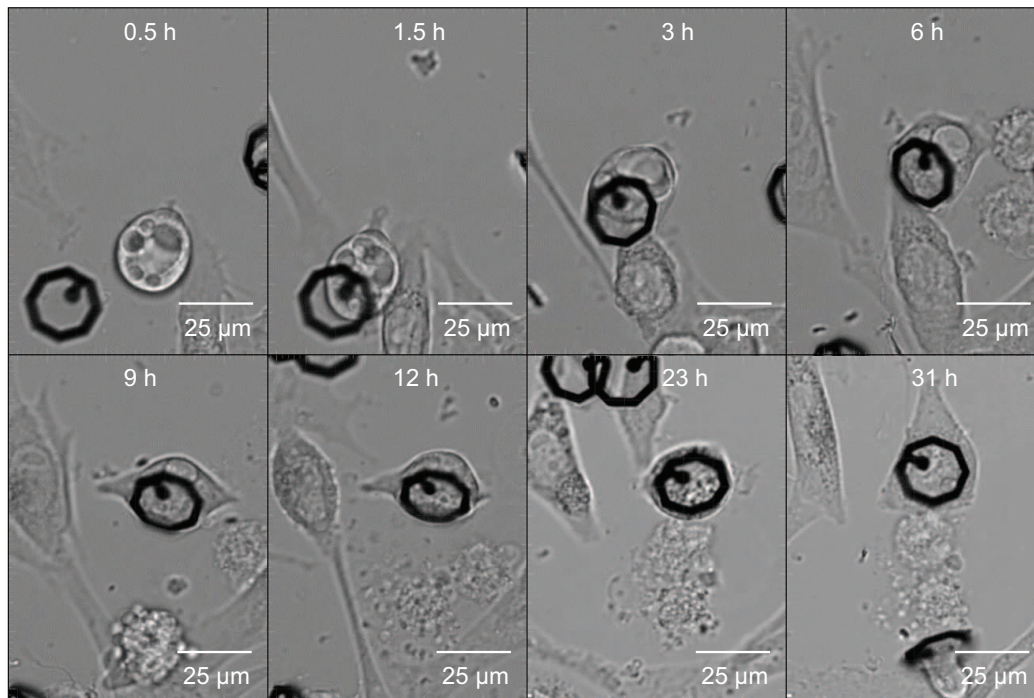


FIG. 6. Time-sequence bright field microscopy images of the cellular uptake and interaction of the house-fabricated RFID. The cells used are human melanoma cells. The complete video is included in the supplemental material [40].

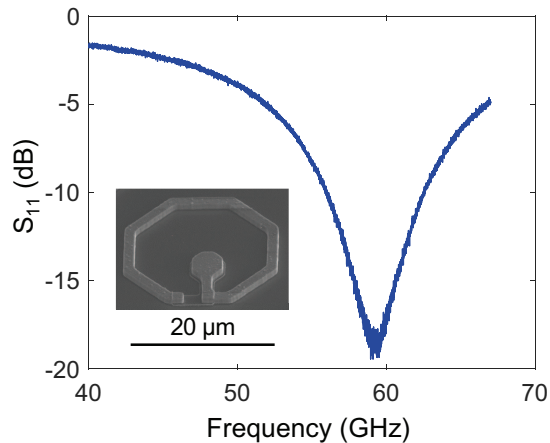


FIG. 7. The measured resonance response of the house-fabricated RFID. The inset shows the tilted top-down scanning electron microscopy (SEM) image of an RFID on the substrate.

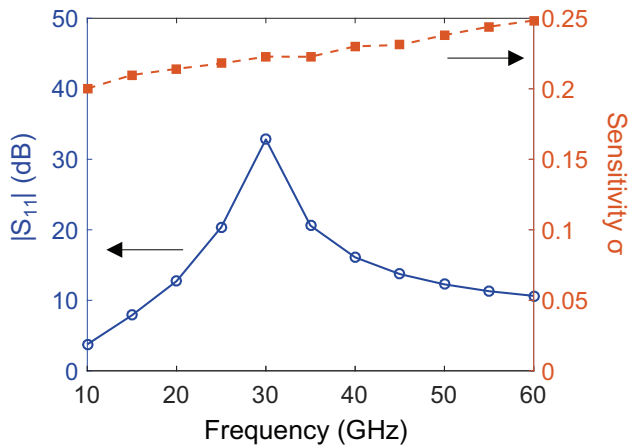


FIG. 8. Characterization of the sensor system for optimal operating frequency. The modeled signal magnitude and sensitivity are plotted from up to 60 GHz, with an ideal loading capacitor for simplicity.

devices is an important design parameter. Previously, frequencies at the MHz range were considered optimal for implantable devices to minimize device dielectric loss in tissue [41]. Mid-field powering method developed in [41–43] shows that frequencies in the low GHz range is optimal for powering up mm-scale devices embedded in body. Since our RFID is much smaller, it is worth examining what the optimal operating frequency should be.

Using the analytical model, the signal magnitude over frequency is plotted in FIG. 8. For the chosen TRX/RFID loop geometries, peak signal magnitude can be obtained around 30 GHz, assuming infinite quality factors of capacitors. However, this low operating frequency requires a large MOM capacitor and the device

area is no longer determined by the inductor loop size. Therefore, only the 55-GHz [40] and 60-GHz versions are fabricated. Congruent with Eq. 6, the theoretical sensitivity [FIG. 8] is relatively constant across frequency. To calculate sensitivity, modeling is carried out with RFID loading (sensor) capacitance C_3 from 80% to 120% of nominal values at intervals of 10%. The resulted resonant frequencies were fitted with least-square method with respect to C_3 to derive the sensitivity. The slightly increased sensitivity favors operation at high frequency.

B. Vertical Detection Range

While the theoretical model sets the RFID to be concentric with the detector, the RFID will float in the microfluidic channel a few micrometers above the detectors when the system is in action. We simulated RFID/TRX with different vertical separations and plotted sensitivity σ and nonlinearity ν with respect to normalized vertical detection range in FIG. 9. The normalized detection range is the ratio between the RFID/TRX distance R to the RFID dimension D [FIG. 1]. The nonlinearity measures the deviation from the ideal linear correlation between input and output [44, 45]. In our case, input is the RFID loading capacitance C_3 while the output is the resonance frequency. We are interested in the input span from 80% to 120% C_3 . The nonlinearity arises not from nonlinear circuit element, but from the mathematical relations between the resonant frequency and the RFID loading capacitance C_3 .

Below 10 μm ($R/D = 0.4$), the lowest resonance trough is used as the marker as designed [FIG. 9(a)]. The sensitivity and nonlinearity are σ_L and ν_L . The signal is prominent and exhibits good linear dependence on capacitance variation. From 10 μm ($R/D = 0.4$) to 17.5 μm ($R/D = 0.7$), the lowest resonance is subdued to a kink for certain loading conditions and it is no longer useful as a signal marker. Note that the higher resonance for 80% to 100% C_3 are highly distinctive and shows good linear shifting [FIG. 9(d)]. However, for a fair comparison, their sensitivities are not plotted due to the reduced linear range. Above 17.5 μm ($R/D = 0.7$), the strongest resonance instead of the lowest resonance shows distinctive and linear correlation with loading capacitance, and it is used as the signal marker for these detection ranges. The sensitivity and nonlinearity are σ_A and ν_A . Beyond 25 μm ($R/D = 1$), the signal is dominated by TRX2 resonance and indifferent to RFID. This is consistent with the magnetic field distribution plotted in FIG. 9(a), where the field decays significantly above 30 μm ($R/D = 1.2$). Please note that although the RFID loop diameter is only 22 μm , we use 25 μm as the device size to normalize the detection range. The extra size is needed to account for the oxide-encapsulation thickness surrounding the RFID loop.

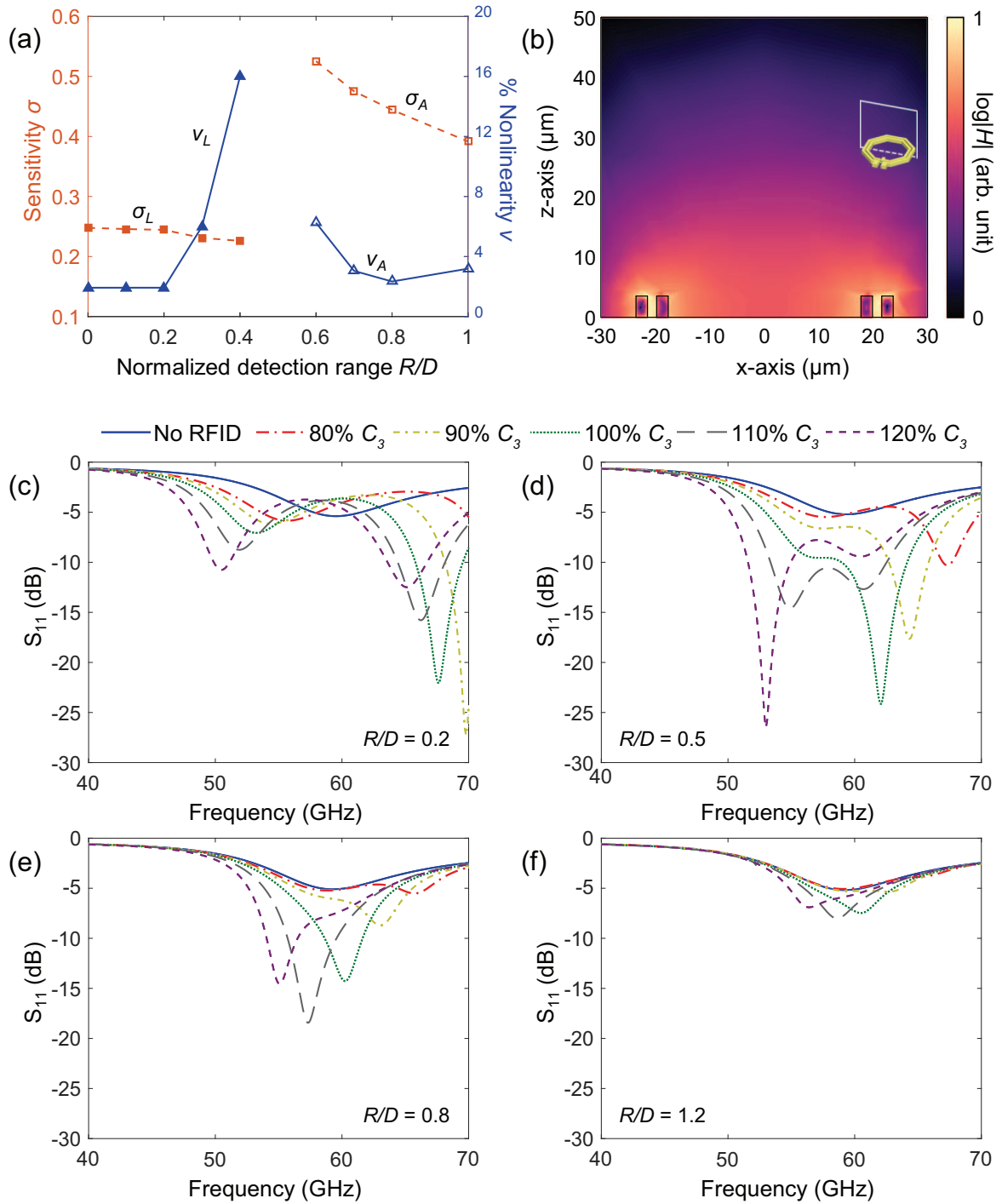


FIG. 9. HFSS-simulated RFID/TRX signal sensitivity σ and nonlinearity ν dependency with respect to normalized detection range R/D . σ_L and ν_L were calculated with the lower split resonance, while σ_A and ν_A with the overall resonance trough. (a) Sensitivity σ and nonlinearity ν trends with respect to R/D . (b) Magnetic-field distribution at xz cross-section through the center of the TRX1 and TRX2. This cross-section is indicated in the inset. The TRX1 and TRX2 are at the bottom of the figure with their wires outlined. The field intensity diminishes above around unit R/D . (c-f) Resonance evolutions as the RFID is gradually elevated away from the TRX. R/D increases from 0.1 to 1.2.

C. Lateral Detection Range

Previous simulation assumes a concentric configuration of the RFID and TRX. In practice, the RFID may be off-centered by a few micrometers in the y direction even with a flow-focusing design for the microfluidic channel. As the RFID is flown through the microfluidic channel along the x-direction, there is a limited time window for obtaining the signal. Therefore, it is desirable that the signal is immune to lateral placement uncertainty. We examine how the relative lateral position of the RFID with respect to the TRX influences the measured signal [FIG. 10]. We performed simulations where the RFID is placed $7.5 \mu\text{m}$ above the TRX detector, and the RFID is moved from the center to the outer edges of the TRX pair at steps of $2.5 \mu\text{m}$. Simulations reveal that when the RFID is within the TRX2 boundary, which represents a moving range of $15 \mu\text{m}$, the signal spectra remain unchanged and different loading conditions can be well distinguished. Once the RFID moves out of that perimeter, signals are deformed and all different conditions generate similar results. In practice, the VNA used has a minimum data acquisition time of 7 ms. If the microfluidic channel has a width of $120 \mu\text{m}$ and a height of $10 \mu\text{m}$, the flow rate needs to be less than 155 nL/min to permit enough time to obtain a stable signal. This flow speed is attainable with most commercial pumps. This simple calculation does not consider various effects such as the flow rate dependency on solution viscosity, flow rate variation across the channel cross-section, or prolonged data acquisition time when more measurement points are taken in a set frequency range. Nonetheless, it serves as a first order approximation to validate the measurement feasibility when a microfluidic channel is integrated with the detector.

V. CONCLUSION

In this work, we present a micron-scale RFID/TRX system based on near-field magnetic resonant coupling as a step toward detecting intra-cellular activities via RF devices. The RFID is minimized to be smaller than typical cells and suitable for embedding into cells. Using two TRX loops, the signal magnitude is improved by more than 40 dB over the configuration with only one TRX loop. The enhanced signal magnitude is essential for the highly lossy operation inside a liquid medium. The RFID/TRX system can be potentially integrated with existing analyte-specific capacitive-based sensors to measure the internal biological and physiological parameters in cells such as pH level [46, 47]. Although the analysis is focused on capacitive sensing, resistive sensing [48–50] is also possible because the resonant coupling is also affected by loop resistances, per discussion in the appendix.

Future work entails *in vitro* measurement of the RFID and TRX with an integrated microfluidic platform. More sophisticated detection algorithm can be developed to combat the non-linearity in the signal due to merged resonance features. The measurement scheme can be further streamlined by replacing the VNA and RF probes with battery powered transceiver circuits.

Appendix A: Resonance Frequency

In a three-port system described by Eq. (1), the input impedance at port 1 can be calculated as

$$\begin{aligned} Z_{in1} &= \frac{V_1}{I_1} = Z_{11} + Z_{2,3 \rightarrow 1} = Z_{11} + Z_{12} \frac{I_2}{I_1} + Z_{13} \frac{I_3}{I_1} \\ &= Z_{11} - Z_{21} \frac{Z_{21}(Z_{33} + Z_{L3}) - Z_{23}Z_{31}}{(Z_{22} + Z_{L2})(Z_{33} + Z_{L3}) - Z_{23}Z_{32}} - Z_{13} \frac{Z_{31}(Z_{22} + Z_{L2}) - Z_{32}Z_{21}}{(Z_{22} + Z_{L2})(Z_{33} + Z_{L3}) - Z_{32}Z_{23}}. \end{aligned} \quad (\text{A1})$$

For our RFID/TRX, each loop has self-inductance L_i and resistance R_i in series. The serial quality factor is Q_i . Ignoring parasitic capacitances, the loops are coupled magnetically with mutual inductance M_{ij} . The impedances in the three TRX/RFID loops can be written as

$$Z_{ii} = j\omega L_i + R_i = j\omega L_i \left(1 + \frac{1}{Q_i}\right), \quad (\text{A2a})$$

$$Z_{ij} = j\omega M_{ij} = j\omega \sqrt{L_i L_j} k_{ij} \quad (\text{A2b})$$

The capacitors C_2 and C_3 on port 2 and 3 resonate with L_2 and L_3 at the same frequency ω_0 :

$$\frac{1}{L_i C_i} = \omega_0^2. \quad (\text{A3})$$

Hence the load impedances are

$$Z_{Li} = -\frac{j}{\omega C_i} = -\frac{j\omega_0^2 L_i}{\omega} \quad (\text{A4})$$

As the matrix is reciprocal, the $Z_{2,3 \rightarrow 1}$ in Eq. (A1) can be re-written as

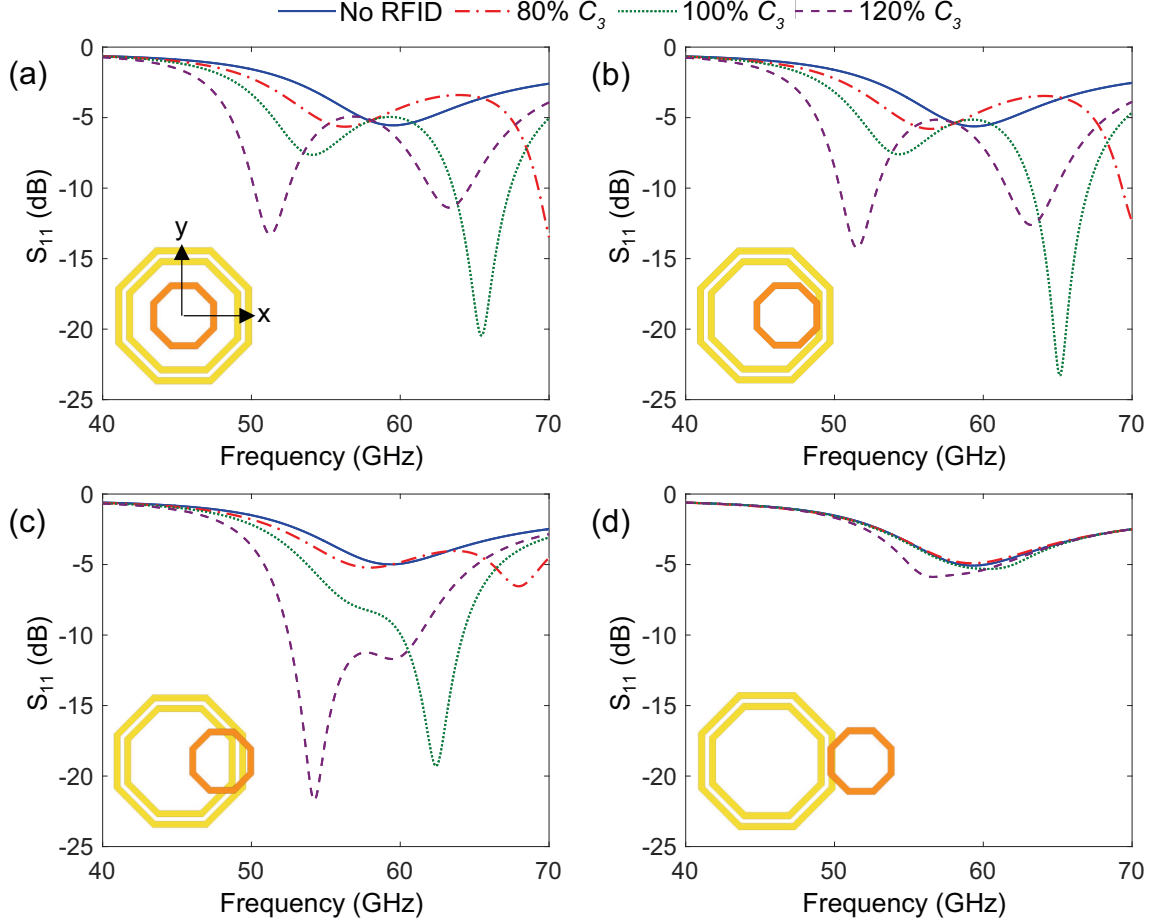


FIG. 10. HFSS-simulated RFID/TRX signal spectra when the RFID is placed at $7.5 \mu\text{m}$ above the TRX for different lateral positions. The RFID starts from the center (a), moves to be right within TRX2 (b), right within TRX1 (c), and finally moves almost out of TRX (d).

$$Z_{2,3 \rightarrow 1} = \frac{-Z_{12}^2(Z_{33} + Z_{L3}) - Z_{13}^2(Z_{22} + Z_{L2}) + 2Z_{12}Z_{23}Z_{13}}{(Z_{22} + Z_{L2})(Z_{33} + Z_{L3}) - Z_{23}^2}. \quad (\text{A5})$$

To arrive at Eq. (5), we can qualitatively simplify the $Z_{2,3 \rightarrow 1}$ expression as the coupling terms $Z_{ij} (i \neq j)$ are small compared to the self-impedance terms:

$$\begin{aligned} Z_{2,3 \rightarrow 1} &\approx \frac{-Z_{12}^2(Z_{33} + Z_{L3}) - Z_{13}^2(Z_{22} + Z_{L2})}{(Z_{22} + Z_{L2})(Z_{33} + Z_{L3})} \\ &= -\frac{Z_{12}^2}{Z_{22} + Z_{33}} - \frac{Z_{13}^2}{Z_{22} + Z_{L2}} \\ &= \frac{|Z_{12}|^2}{Z_{22} + Z_{33}} + \frac{|Z_{13}|^2}{Z_{22} + Z_{L2}}. \end{aligned} \quad (\text{A6})$$

The last step above uses the fact that Z_{12} and Z_{13} are imaginary.

To numerically solve for the resonance frequencies of TRX/RFID, we can directly express Z_{in1} as a function of frequency ω according to Eq. (A1-A4), substitute it

into Eq. (2), and find the frequencies corresponding to the local minima of $|\Gamma|$.

To establish design intuition, we need a simple closed-form formula for the resonant frequencies in terms of the known impedances. We find that the RFID/TRX resonances can be approximated as the coupled resonances of TRX2 and RFID, as long as that the quality factors are high and resistances are thus negligible. This two-port TRX2 and RFID network \mathbf{Z}_r is

$$\begin{aligned} &\begin{bmatrix} Z_{22} + Z_{L2} & Z_{23} \\ Z_{23} & Z_{33} + Z_{L3} \end{bmatrix} \\ &\approx \begin{bmatrix} j(\omega L_2 - \frac{\omega_0^2 L_2}{\omega}) & j\omega\sqrt{L_2 L_3} k_{23} \\ j\omega\sqrt{L_2 L_3} k_{23} & j(\omega L_3 - \frac{\omega_0^2 L_3}{\omega}) \end{bmatrix} \end{aligned} \quad (\text{A7})$$

The resonant frequencies can be found by setting its determinant to 0:

$$\left[-\left(\omega - \frac{\omega_0^2}{\omega}\right)\left(\omega - \frac{\omega_0^2}{\omega}\right) + \left(\omega k_{23}\right)^2 \right] L_2 L_3 = 0 \quad (\text{A8})$$

The non-trivial roots are the split low and high resonant frequencies:

$$\omega_L = \frac{\omega_0}{\sqrt{1+k_{23}}}, \quad (\text{A9a})$$

$$\omega_H = \frac{\omega_0}{\sqrt{1-k_{23}}}. \quad (\text{A9b})$$

This resonance calculation is equivalent to maximizing Z_{in1} as the determinant is the denominator in Eq. (A1) when resistances of the RFID and TRX2 are negligible.

When TRX2 and RFID resistances are large, the splitting frequency formula of two damped resonant elements is of high polynomial degree in general [30] and does not have roots that are easy to interpret. The formula can be simplified to bi-quadratic with straightforward solutions only when $Z_{22} = \alpha Z_{33}$ [30] and most papers present the result when Z_{22} is identical with Z_{33} or when numeric values are given [31, 32]. At the same time, the splitting can only occur when the coupling coefficient exceeds the critical splitting coupling which increases with resistances [29, 30]. With larger resistances, it is harder to overcome the splitting coupling, the two resonant elements move from an over-coupled regime to an under-coupled regime, and the two resonances merge into one. This single resonance is less prominent and harder to detect compared to the splitting counterparts. Hence, we restrict ourselves to over coupled RFID and TRX2 with negligible resistances.

Appendix B: Signal Enhancement

With the approximated resonance frequencies, we can calculate input impedance Z_{in1} and signal magnitude. Take the low resonance ω_L for example. The denominator of Eq. A5 is:

$$\begin{aligned} d &= \frac{\omega_L^2 L_2 L_3}{Q_2 Q_3} [-jk_{23}(Q_2 + Q_3) + 1] \\ &\approx \frac{\omega_L^2 L_2 L_3}{Q_2 Q_3} [-jk_{23}(Q_2 + Q_3)]. \end{aligned} \quad (\text{B1})$$

The corresponding numerator is:

$$\begin{aligned} n &= \omega_L^3 L_1 L_2 L_3 \left[k_{12}^2 \left(\frac{1}{Q_3} - jk_{23} \right) \right. \\ &\quad \left. + k_{13}^2 \left(\frac{1}{Q_2} - jk_{23} \right) - 2jk_{12}k_{13}k_{23} \right] \\ &\approx \omega_L^3 L_1 L_2 L_3 [-jk_{23}(k_{12}^2 + k_{13}^2 + 2k_{12}k_{13})]. \end{aligned} \quad (\text{B2})$$

The approximations above are valid in the high-Q configuration. Dividing the numerator by the denominator, we get the approximated $Z_{2,3 \rightarrow 1}$, which is a real impedance. This real impedance can improve the matching of port 1 and the source and boost the signal strength. The total real input impedance is

$$\begin{aligned} \Re Z_{in1} &= \Re Z_1 + Z_{2,3 \rightarrow 1} \\ &= R_1 + \omega_L L_1 (k_{12}^2 + k_{13}^2 + 2k_{12}k_{13}) \frac{1}{1/Q_2 + 1/Q_3}. \end{aligned} \quad (\text{B3})$$

Similarly, the real input impedance at the high resonance is

$$\begin{aligned} \Re Z_{in1} &= \Re Z_1 + Z_{2,3 \rightarrow 1} \\ &= R_1 + \omega_H L_1 (k_{12}^2 + k_{13}^2 - 2k_{12}k_{13}) \frac{1}{1/Q_2 + 1/Q_3}. \end{aligned} \quad (\text{B4})$$

Appendix C: Sensitivity

Sensitivity σ is the derivative of Eq. (A9) with respect to C_3 . Take the lower resonance sensitivity for instance. First rewrite it in terms of L and C :

$$\omega_L = \frac{1}{\sqrt{(1+k_{23})(L_3 C_3)}}. \quad (\text{C1})$$

Taking partial derivative with respect to C_3

$$\frac{\partial \omega_L}{\partial C_3} = -\frac{1}{2\sqrt{(1+k_{23})L_3 C_3^3}} = -\frac{1}{2\sqrt{1+k_{23}}} \frac{\omega_0}{C_3}. \quad (\text{C2})$$

Dividing by ω_0/C_3 , sensitivity near the lower resonance is

$$\sigma_L = \frac{\Delta f/f}{\Delta C_3/C_3} = -\frac{1}{\sqrt{1+k_{23}}}. \quad (\text{C3})$$

Similarly, sensitivity near the higher resonance is

$$\sigma_H = -\frac{1}{\sqrt{1-k_{23}}}. \quad (\text{C4})$$

ACKNOWLEDGMENTS

We thank Professor Thomas H. Lee of the Department of Electrical Engineering at Stanford University for providing RF measurement equipment. This work is supported in part by Stanford Bio-X Seed Grant, and the Air Force Office of Scientific Research (MURI: Atomically-Thin Systems That Unfold, Interact and Communicate at the Cellular Scale). X. Hu received funding from the Stanford Graduate Fellowship and M.X. Yang from the National Science Foundation. The cell imaging is conducted at School of Engineering Shriram Center Cell Sciences Imaging Facility at Stanford University.

-
- [1] R. Gómez-Martínez, A. M. Hernández-Pinto, M. Duch, P. Vázquez, K. Zinoviev, J. Enrique, J. Esteve, T. Suárez, and J. A. Plaza, "Silicon chips detect intracellular pressure changes in living cells," *Nat. Nanotech.* **8**, 517 (2013).
- [2] J. Han and K. Burgess, "Fluorescent indicators for intracellular pH," *Chem. Rev.* **110**, 2709 (2009).
- [3] S. Saha, V. Prakash, S. Halder, K. Chakraborty, and Y. Krishnan, "A pH-independent DNA nanodevice for quantifying chloride transport in organelles of living cells," *Nat. Nanotech.* **10**, 645 (2015).
- [4] W. Wang, S. Li, L. Mair, S. Ahmed, T. J. Huang, and T. E. Mallouk, "Acoustic propulsion of nanorod motors inside living cells," *Angewandte Chemie International Edition* **53**, 3201 (2014).
- [5] P. Burke and C. Rutherglen, "Towards a single-chip, implantable RFID system: is a single-cell radio possible?" *Biomed Microdevices* **12**, 589 (2010).
- [6] S.-H. Cho, N. Xue, L. Cauller, W. Rosellini, and J.-B. Lee, "A SU-8-based fully integrated biocompatible inductively powered wireless neurostimulator," *J. Microelectromech. Syst.* **22**, 170 (2013).
- [7] J. S. Ho, A. J. Yeh, E. Neofytou, S. Kim, Y. Tanabe, B. Patlolla, R. E. Beygui, and A. S. Y. Poon, "Wireless power transfer to deep-tissue microimplants," *PNAS* **111**, 7974 (2014).
- [8] Y.-T. Liao, H. Yao, A. Lingley, B. Parviz, and B. P. Otis, "A 3-CMOS glucose sensor for wireless contact-lens tear glucose monitoring," *IEEE J. Solid-State Circuits* **47**, 335 (2012).
- [9] H. Yu, C.-M. Tang, and R. Bashirullah, "An asymmetric RF tagging IC for ingestible medication compliance capsules," in *Radio Frequency Integrated Circuits Symposium (RFIC)* (IEEE, 2009) p. 101.
- [10] P. J. Burke, S. Li, and Z. Yu, "Quantitative theory of nanowire and nanotube antenna performance," *IEEE Trans. Nanotechnol.* **5**, 314 (2006).
- [11] S. Ozeri and D. Shmilovitz, "Ultrasonic transcutaneous energy transfer for powering implanted devices," *Ultrasonics* **50**, 556 (2010).
- [12] I. Ladabaum, X. Jin, H. T. Soh, A. Atalar, and B. T. Khuri-Yakub, "Surface micromachined capacitive ultrasonic transducers," *IEEE Trans. Ultrason., Ferroelect., Freq. Control* **45**, 678 (1998).
- [13] K. Chen, H.-S. Lee, A. P. Chandrakasan, and C. G. Sodini, "Ultrasonic imaging transceiver design for CMUT: A three-level 30-vpp pulse-shaping pulser with improved efficiency and a noise-optimized receiver," *IEEE J. Solid-State Circuits* **48**, 2734 (2013).
- [14] H. J. Lee, K. K. Park, M. Kupnik, O. Oralkan, and B. T. Khuri-Yakub, "Chemical vapor detection using a capacitive micromachined ultrasonic transducer," *Anal. Chem.* **83**, 9314 (2011).
- [15] Q. Stedman, K. K. Park, and B. T. Khuri-Yakub, "CMUT chip with integrated temperature and pressure sensors," in *International Ultrasonics Symposium (IUS)* (IEEE, 2016).
- [16] M. Ferrari, V. Ferrari, M. Guizzetti, and D. Marioli, "An autonomous battery-less sensor module powered by piezoelectric energy harvesting with RF transmission of multiple measurement signals," *Smart Mater. Struct.* **18**, 085023 (2009).
- [17] J. Charthad, M. J. Weber, T. C. Chang, and A. Arbabian, "A mm-sized implantable medical device (IMD) with ultrasonic power transfer and a hybrid bi-directional data link," *IEEE J. Solid-State Circuits* **50**, 1741 (2015).
- [18] X. Hu, W. Li, M. X. Yang, K. Aggarwal, A. S. Y. Poon, and H.-S. P. Wong, "Mini-RFID: toward implantable cellular sensors," in *The 19th International Conference on Miniaturized Systems for Chemistry and Life Sciences (MicroTAS, 2015)* p. 2126.
- [19] L. Y. Chen, K. B. Parizi, H. Kosuge, K. M. Milaninia, M. V. McConnell, H.-S. P. Wong, and A. S. Y. Poon, "Mass fabrication and delivery of 3D multilayer tags into living cells," *Sci. Rep.* **3**, 2295 (2013).
- [20] S. D. Barman, A. W. Reza, N. Kumar, M. E. Karim, and A. B. Munir, "Wireless powering by magnetic resonant coupling: Recent trends in wireless power transfer system and its applications," *Renew. Sust. Energ. Rev.* **51**, 1525 (2015).
- [21] J. Kim, H.-C. Son, K.-H. Kim, and Y.-J. Park, "Efficiency analysis of magnetic resonance wireless power transfer with intermediate resonant coil," *IEEE Antennas Wireless Propag. Lett.* **10**, 389 (2011).
- [22] S. Bushnaq, M. Ikeda, and K. Asada, "Range extension of inductive coupling communication using multi-stage resonance," in *International Symposium on Communications and Information Technologies (ISCIT)* (IEEE, 2012) p. 758.
- [23] S. Bai, D. C. Ng, E. Skafidas, and I. M. Y. Mareels, "Generalized maximum efficiency theory on multi-stage inductive coupling," in *Progress in Electromagnetics Research Symposium (PIERS)* (PIERS, 2010) p. 245.
- [24] R. E. Hamam, A. Karalis, J. D. Joannopoulos, and M. Soljačić, "Efficient weakly-radiative wireless energy transfer: An EIT-like approach," *Ann. Phys.* **324**, 1783 (2009).
- [25] A. S. Y. Poon, "A general solution to wireless power transfer between two circular loops," *Prog. Electromagn. Res.* **148**, 171 (2014).
- [26] Mathworks, MATLAB, Release 2015.b.
- [27] D. M. Pozar, in *Microwave Engineering* (John Wiley & Sons, Hoboken, New Jersey, 2009) Chap. 2, p. 91, 3rd ed.
- [28] H. A. Haus, in *Waves and fields in optoelectronics* (Prentice Hall, Upper Saddle River, New Jersey, 1984) Chap. 7, p. 211, 1st ed.
- [29] R. Huang, B. Zhang, D. Qiu, and Y. Zhang, "Frequency splitting phenomena of magnetic resonant coupling wireless power transfer," *IEEE Trans. Magn.* **50**, 1 (2014).
- [30] W.-Q. Niu, J.-X. Chu, W. Gu, and A.-D. Shen, "Exact analysis of frequency splitting phenomena of contactless power transfer systems," *IEEE Trans. Circuits Syst. I, Reg. Papers* **60**, 1670 (2013).
- [31] M. Kiani and M. Ghovanloo, "The circuit theory behind coupled-mode magnetic resonance-based wireless power transmission," *IEEE Trans. Circuits Syst. I, Reg. Papers* **59**, 2065 (2012).
- [32] Y. Zhang and Z. Zhao, "Frequency splitting analysis of two-coil resonant wireless power transfer," *IEEE Antennas Wireless Propag. Lett.* **13**, 400 (2014).

- [33] ANSYS, ANSYS[®] Electronics Desktop, Release 2015.2.
- [34] W. K. W. Ali and S. H. Al-Charchafchi, "Using equivalent dielectric constant to simplify the analysis of patch microstrip antenna with multi-layer substrates," in *Antennas and Propagation Society International Symposium (APSURSI)*, Vol. 2 (IEEE, 1998) p. 676.
- [35] TSMC, tsmc.com/english/dedicatedFoundry/index.htm.
- [36] Lorentz Solutions, www.lorentzsolution.com.
- [37] Cadence design systems, www.cadence.com.
- [38] B. Zhang, Y.-Z. Xiong, L. Wang, S. Hu, and J. L.-W. Li, "De-embedding of on-chip inductor at millimeter-wave range," *Jpn. J. Appl. Phys.* **51**, 086602 (2012).
- [39] D. A. Frickey, "Conversions between S, Z, Y, H, ABCD, and T parameters which are valid for complex source and load impedances," *IEEE Trans. Microw. Theory Techn.* **42**, 205 (1994).
- [40] See Supplemental Material at URL for a video showing RFID internalization and cell persistence as well as measurement results of 55-GHz RFID/TRX.
- [41] S. Kim, J. S. Ho, and A. S. Y. Poon, "Midfield wireless powering of subwavelength autonomous devices," *Phys. Rev. Lett.* **110**, 203905 (2013).
- [42] A. S. Y. Poon, S. O'Driscoll, and T. H. Meng, "Optimal operating frequency in wireless power transmission for implantable devices," in *29th Annual International Conference of the IEEE Engineering in Medicine and Biology Society (EMBS)* (IEEE, 2007) p. 5673.
- [43] A. Ma and A. S. Y. Poon, "Midfield wireless power transfer for bioelectronics," *IEEE Circuits Syst. Mag.* **15**, 54 (2015).
- [44] J. J. Carr, in *Sensors and circuits* (Prentice Hall, Englewood Cliffs, New Jersey, 1993) Chap. 1, p. 13, 1st ed.
- [45] National Instruments, "Sensor terminology," www.ni.com/white-paper/14860/en/.
- [46] B. M. P. Ramos, A. D. Sanchez, and J. M. Reyes, "Chemical analysis of thin ALD-Al₂O₃ films and their applications as pH-sensitive layers in CMOS-compatible ion-sensitive capacitors (ISCAP)," in *SENSORS* (IEEE, 2015).
- [47] C. Occhiuzzi, A. Ajovalasit, M. A. Sabatino, C. Dispenza, and G. Marrocco, "RFID epidermal sensor including hydrogel membranes for wound monitoring and healing," in *International Conference on RFID (RFID)* (IEEE, 2015) p. 182.
- [48] H. Tsuruta, S. Matsui, K. Oka, T. Namba, M. Shinngu, and M. Nakamura, "Quantitation of IL-1 β mRNA by a combined method of RT-PCR and an ELISA based on ion-sensitive field effect transistor," *J. Immunol. Methods* **180**, 259 (1995).
- [49] K. B. Parizi, A. J. Yeh, A. S. Y. Poon, and H.-S. P. Wong, "Exceeding Nernst limit (59mV/pH): CMOS-based pH sensor for autonomous applications," in *International Electron Devices Meeting (IEDM)* (IEEE, 2012) p. 24.7.1.
- [50] P. Gou, N. D. Kraut, I. M. Feigel, H. Bai, G. J. Morgan, Y. Chen, Y. Tang, K. Bocan, J. Stachel, L. Berger, M. Mickle, E. Sejdić, and A. Star, "Carbon nanotube chemiresistor for wireless pH sensing," *Sci. Rep.* **4**, 4468 (2014).